AGU100 ADVANCING EARTH AND SPACE SCIENCE

Geophysical Research Letters

RESEARCH LETTER
10.1029/2018GL081216

Key Points:
- Multiple crescents in an electron distribution function are due to meandering motion and acceleration by the reconnection electric field
- Shape of stripes is obtained as a function of the reconnection electric field
- Applying the theory to observation data in Earth's magnetotail, the reconnection electric field is estimated

Correspondence to:
N. Bessho,
naoki.bessho@nasa.gov

Citation:
Bessho, N., Chen, L.-J., Wang, S., & Hesse, M. (2018). Effect of the reconnection electric field on electron distribution functions in the diffusion region of magnetotail reconnection. *Geophysical Research Letters*, *45*, 12,142–12,152. https://doi.org/10.1029/2018GL081216

Received 5 NOV 2018
Accepted 8 NOV 2018
Accepted article online 12 NOV 2018
Published online 28 NOV 2018

Effect of the Reconnection Electric Field on Electron Distribution Functions in the Diffusion Region of Magnetotail Reconnection

N. Bessho[1,2], L.-J. Chen[1,2], S. Wang[1,2], and M. Hesse[3,4]

[1]Department of Astronomy, University of Maryland, College Park, MD, USA, [2]Heliophysics Science Division, NASA Goddard Space Flight Center, Greenbelt, MD, USA, [3]Birkeland Centre for Space Science, University of Bergen, Bergen, Norway, [4]Southwest Research Institute, San Antonio, TX, USA

Abstract Electron distribution functions in the electron diffusion region during symmetric magnetic reconnection are investigated by means of theory and fully kinetic simulations. Crescent-like striations are formed in distribution functions in the velocity plane perpendicular to the magnetic field. Using an analytical current sheet, we solve the equation of motion for electrons, and derive the shape of a crescent distribution, as a function of the distance from the neutral line, field gradients, and the reconnection electric field. Each crescent is tilted in the velocity plane because of the acceleration by the reconnection electric field, and multiple stripes appear due to multiple meandering bounces. Applying the theory to distribution functions observed in Earth's magnetotail, we deduce the amplitude of the reconnection electric field.

Plain Language Summary Magnetic reconnection is a mechanism to rapidly release magnetic energy, causing, for example, magnetic substorms in Earth's magnetosphere. Understanding particle motion and energy release during reconnection is highly important in space plasma physics. Reconnection can occur where electrons are moving back and forth across a current sheet. When reconnection occurs, electrons are accelerated by the electric field generated by reconnection. Evidence of such electron motion and acceleration should be seen in particle data in spacecraft orbiting Earth. In this study, using computer simulations and space observations by National Aeronautics and Space Administration's Magnetospheric Multiscale Mission, we demonstrate characteristic shapes in the electron data from reconnection in Earth's nightside magnetosphere. We derive a formula to explain multiple stripes seen in the electron data. The theory successfully explains the simulation data. This formula is applied to space observation data to extract the electric field amplitude during magnetic reconnection. Direct measurement of this electric field is challenging because of its small amplitude and the presence of other simultaneous fluctuations. Our method can be used to estimate the electric field from electron data.

1. Introduction

In space observations such as in Earth's magnetosphere, velocity distribution functions (VDFs) for ions and electrons provide us useful information about the physics working on local plasmas. For example, in National Aeronautics and Space Administration's Magnetospheric Multiscale (MMS) mission (Burch et al., 2015), electron VDFs with a crescent shape have been detected as evidence of fast reconnection (Argall et al., 2018; Burch et al., 2016; Burch & Phan, 2016; Chen, Hesse, Wang, Gershman, et al., 2016; Chen et al., 2017; Genestreti et al., 2017, 2018; Norgren et al., 2016; Phan et al., 2016; Rager et al., 2018).

Crescent electron VDFs are a signature of reconnection in Earth's magnetopause (Bessho et al., 2016, 2017; Cassak et al., 2017; Chen, Hesse, Wang, Bessho, et al., 2016; Egedal et al., 2016; Hesse et al., 2014, 2016; Lapenta et al., 2017; Shay et al., 2016; Zenitani et al., 2017). From crescent VDFs, we can extract information of the electron diffusion region (EDR). For example, the curvature of a crescent is related with the distance from the magnetic neutral line (Bessho et al., 2016); therefore, we can estimate the EDR thickness from crescent VDFs. Also, the reconnection electric field can be estimated from the crescent width (Bessho et al., 2017).

In contrast, in Earth's magnetotail reconnection, where field strength is symmetric across a current sheet, crescent VDFs are still expected in the EDR because of electron meandering motion. Test particle analysis (Divin et al., 2010) and kinetic simulations (Hesse et al., 2018; Shuster et al., 2015) show crescent-like electron VDFs with multiple stripes in symmetric reconnection. Also, in a recent observation by MMS of an

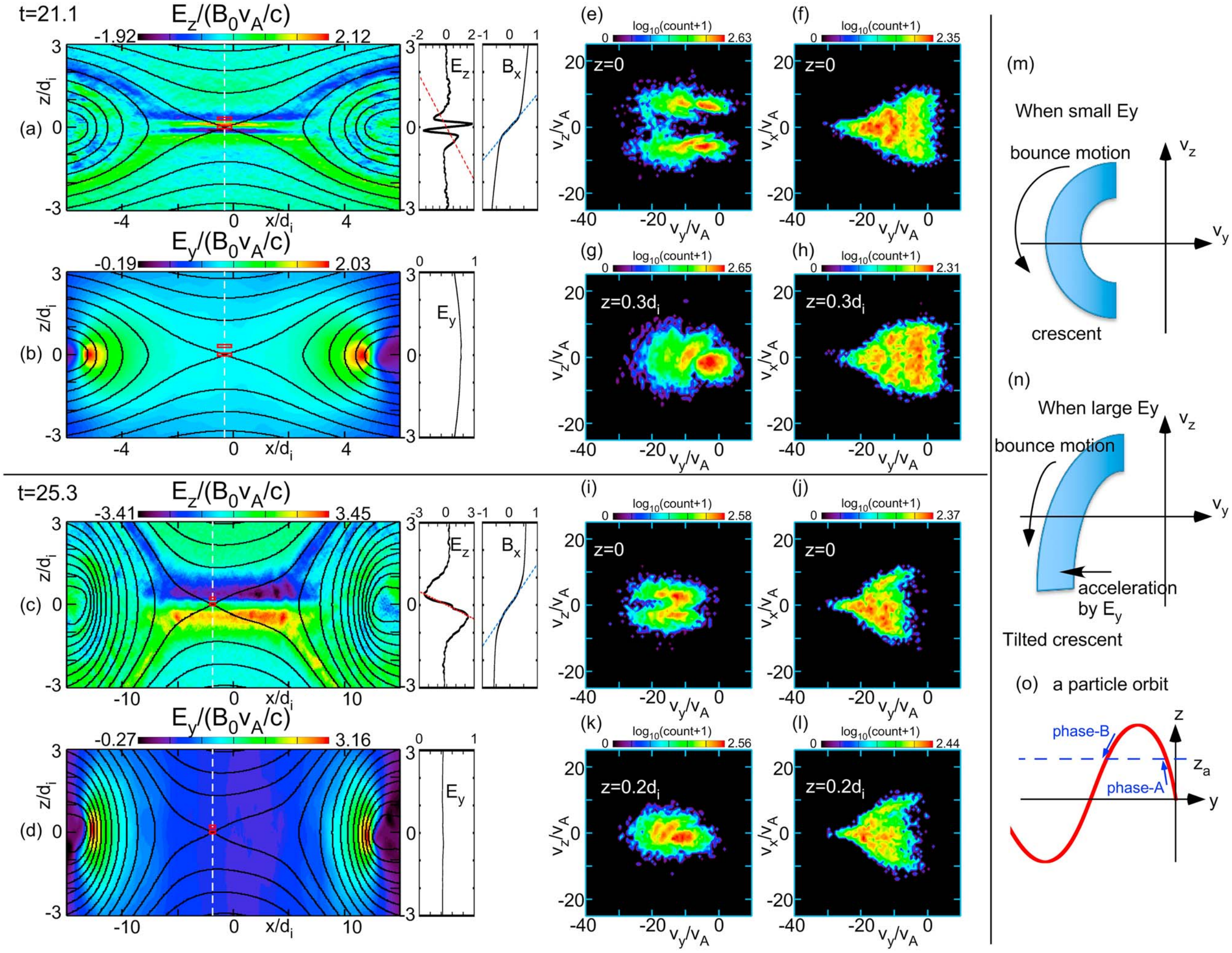

Figure 1. Contours of E_z and E_y: (a) and (b) at $\Omega_i t = 21.1$ and (c) and (d) at $\Omega_i t = 25.3$. (Right panels in a–d) Cuts of E_z, B_x, and E_y across the white dashed line. Dashed red and blue lines: the linear regression lines using data in $|z| < 0.5d_i$ to estimate the slopes. (e–h) and (i–l) Reduced electron velocity distribution functions (accumulated during 10 time steps ~$8\times10^{-3}\Omega_i^{-1}$) in the red boxes in the contours, at the X-line ($z = 0$) and away from the X-line (at $z = 0.3d_i$ for $\Omega_i t = 21.1$, and $z = 0.2d_i$ for $\Omega_i t = 25.3$). (m) and (n) Diagram showing an almost symmetric crescent (m) and an asymmetric crescent (n). (o): particle orbit in *y-z*.

EDR-crossing in Earth's magnetotail (Torbert et al., 2018), crescent electron VDFs with multiple stripes have been detected.

In this letter, we discuss the mechanism of multiple crescents in symmetric reconnection, by means of theory and 2.5-dimensional particle-in-cell (PIC) simulations. In our previous study (Bessho et al., 2014), we discussed the electron VDF on the X-line, which shows multiple stripes. We will extend the above study to a VDF slightly away from the X-line in the inflow direction.

Quantifying the reconnection electric field based on MMS observations has important impact. We will demonstrate that the comparison of the crescent separation in electron VDFs with theory is useful to derive the reconnection electric field from VDF data.

2. PIC Simulation of Magnetotail Reconnection and Multiple Crescents in Electron VDFs

We study magnetotail reconnection without guide field by means of 2.5-D PIC simulations (same initial setup in Bessho et al., 2014) using a Harris sheet: magnetic field $B_x = B_0 \tanh(z/w)$ and density $n = n_0 \mathrm{sech}^2(z/w) + n_b$, where $w = 0.5d_i$ (d_i: ion skin depth with n_0). The system size is $L_x \times L_z = 51.2d_i \times 25.6d_i$ ($1d_i = 20$ grids). The mass ratio $m_i/m_e = 50$, the temperature ratio $T_i/T_e = 1$, the ratio of the plasma frequency (for n_0) to the electron cyclotron frequency (for B_0) ω_{pe}/Ω_e = 6.0 (Alfvén speed: v_A/c = 1/42.4, c: the light speed), and n_b = 0.0375n_0 (where n_0 corresponds to 3,840 particles per cell). All the boundaries are open (Daughton et al., 2006). We also performed a run with m_i/m_e = 200, and the result is qualitatively similar. Thus, we will only show the result with m_i/m_e = 50.

Figures 1a–1b show the electric fields E_z and E_y at $\Omega_i t$ = 21.1 (Ω_i: ion cyclotron frequency with B_0). The reconnection electric field E_y at the X-line $x = -0.3d_i$ and $z = 0$ is $0.76B_0v_A/c$ (where v_A is based on n_0), significantly higher than $0.2B_0v_A/c$ in the GEM challenge (Birn et al., 2001), because of a small background density $n_b = 0.0375n_0$. On the other hand, using the values in the EDR edge ($B_x = 0.43B_0$ at $|z| \sim 0.8d_i$ and $v_{xe} = 5.8v_A$ at the electron outflow maximum), the normalized rate in unit of B_xv_{xe}/c is 0.31.

E_z shows a layered structure in $|z| < d_i$ near the X-line. The outermost layers show negative (positive) values in $z > 0.22d_i$ ($z < -0.22d_i$), and the inner layers show the reversed signs: positive (negative) in $0 < z < 0.22d_i$ ($-0.22d_i < z < 0$). This innermost inversion layer (Chen et al., 2011) is due to the meandering electrons. The cuts of E_z, E_y, and B_x are shown in the right panels of contours, across the white dashed line.

The time $\Omega_i t$ = 21.1 is near the peak reconnection rate, and at later time the inversion layer disappears. Figures 1c–1d are E_z and E_y at $\Omega_i t$ = 25.3, where E_y at the X-line drops to $0.43B_0v_A/c$. As a result of the EDR expansion (EDR size increase), the E_z-layer becomes broader, and only a bipolar Hall field remains.

The two red boxes in Figures 1a–1d are where we measure electron VDFs in Figures 1e–1l. The lower red box is at the X-line, and the upper one is at $x = -0.3d_i$ and $z = 0.3d_i$ for $\Omega_i t$ = 21.1, and $x = -1.65d_i$ and $z = 0.2d_i$ for $\Omega_i t$ = 25.3. The box size is $0.5d_i$ and $0.1d_i$ in the x and z directions, respectively.

Figures 1e–1l show reduced VDFs. The X-line VDF (Figures 1e and 1f for $\Omega_i t$ = 21.1, also Figures 1i and 1j for $\Omega_i t$ = 25.3) shows two layers in v_y-v_z, and a triangular structure in v_y-v_x, similar to previous studies (Bessho et al., 2014; Ng et al., 2012, 2011; Shuster et al., 2015). The striations in $v_y < 0$ in Figure 1f are due to electron meandering across the current sheet and acceleration by E_y.

Slightly away from the X-line, the VDFs show multiple crescents in v_y-v_z (Figures 1g and 1k). These crescents are not symmetric across $v_z = 0$, but v_y in $v_z < 0$ is more negative than v_y in $v_z > 0$. In other words, crescents are tilted.

The tilted crescents are due to acceleration by E_y. A crescent-VDF is due to meandering motion (Figure 1o, the red curve shows a trajectory in y-z), and if there were no E_y, only one symmetric crescent across $v_z = 0$ would exist. In asymmetric reconnection, where E_y effects are secondary, an almost symmetric crescent forms (Figure 1m; Bessho et al., 2016; Chen, Hesse, Wang, Bessho, et al., 2016; Hesse et al., 2014; Shay et al., 2016). In contrast, in symmetric reconnection, E_y effects are pronounced. Let us discuss a VDF at a general position $z = z_a > 0$, using Figure 1o. At $z = z_a$, electrons in phase-A have $v_z > 0$, coming from $z < z_a$, while electrons in phase-B have $v_z < 0$, returning to $z = z_a$ after passing the z-maximum, $z = z_m$. Therefore, the electrons with $v_z < 0$ in phase-B spent more time being accelerated by E_y, resulting in more negative v_y (Figure 1n).

3. Theory of Multiple Crescents in a VDF

We discuss electron meandering and derive an equation for stripes (crescents) in a VDF. We assume that fields depend only on z, given as $\boldsymbol{B} = (bz, 0, 0)$, and $\boldsymbol{E} = (0, E_r, -kz)$, where b and $-k$ are the slopes of B_x and E_z (neglecting the innermost inversion layer near z = 0), respectively, and E_r is a uniform reconnection electric field.

Let us discuss the electron meandering (with its rest mass m) from $z = z_0 = 0$ (the subscript 0 represents the value at $t = 0$) in the same way as Speiser (1965), Divin et al. (2010), Ng et al. (2012), and Bessho et al. (2014). The equations of motion for y and z are

$$m\frac{\mathrm{d}\gamma v_y}{\mathrm{d}t} = -eE_r - \frac{e}{c}v_z bz, \tag{1}$$

$$m\frac{\mathrm{d}\gamma v_z}{\mathrm{d}t} = ekz + \frac{e}{c}v_y bz, \tag{2}$$

where γ is the Lorentz factor. We assume that $v_z^2 \ll v_y^2 \ll c^2$ and $\gamma \sim 1 + (1/2)(v_y/c)^2$.

From equation (1) using $v_z = \mathrm{d}z/\mathrm{d}t$, we obtain

$$\gamma v_y = v_{y0} - \frac{eE_r}{m}t - \frac{eb}{2mc}z^2, \tag{3}$$

where we assume that γ_0~1. Substituting equation (3) into equation (2), we obtain

$$\frac{\mathrm{d}^2 z}{\mathrm{d}t^2} = -\frac{e^2 E_r b}{m^2 c} z\left(t - \frac{m v_{y0}}{eE_r} - \frac{mck}{eE_r b}\right) - \frac{e^2 b^2}{2m^2 c^2}z^3 + O(\gamma - 1), \tag{4}$$

where the last term represents terms of the order of $\gamma - 1$. Discussing the leading order z-motion near $z = 0$, we neglect the last two terms ($\propto z^3$ and $O(\gamma - 1)$). The solution of equation (4) is expressed using two Airy functions (and constants c_1 and c_2):

$$z = c_1 \mathrm{Ai}\left(-a^{1/3}s\right) + c_2 \mathrm{Bi}\left(-a^{1/3}s\right), \tag{5}$$

where a and s are

$$a = \frac{e^2 E_r b}{m^2 c}, \tag{6}$$

$$s = t - \frac{m}{eE_r}\left(v_{y0} + \frac{ck}{b}\right), \tag{7}$$

and Ai(x) and Bi(x) represent Airy functions with $x = -a^{1/3}s$. A quarter of the meandering period is roughly t_{qm}~$a^{1/3}$.

From equation (5) we can obtain the relationship between v_y and v_z (details are in Appendix A). Substituting equation (A8) into (A7), we have v_z as a function of v_y:

$$v_z \sim z\left(\frac{eb}{mc}\right)^{1/2}\left(-\gamma v_y - \frac{eb}{2mc}z^2 - \frac{ck}{b}\right)^{1/2} \times \cot\left\{\frac{2}{3}\left(\frac{eb}{mc}\right)^{1/2}\frac{m}{eE_r}\left[\left(-\gamma v_y - \frac{eb}{2mc}z^2 - \frac{ck}{b}\right)^{3/2} - \left(-v_{y0} - \frac{ck}{b}\right)^{3/2}\right]\right\}, \tag{8}$$

where $\gamma = 1 + (1/2)(v_y/c)^2$. This is based on an approximation of Airy functions for $s > 0$ (see Appendix A), valid for $v_{y0} < -ck/b$. For the other case ($v_{y0} \geq -ck/b$), we must use equation (A11) combined with equation (A8).

Physically, equation (8) represents a particle's meandering motion and acceleration by E_r. Let us consider a particle arriving at $z = z_a$ at $t = t_a$. Equation (8) is in a form $v_z = z_a T^{-1} \times \cot f(v_y)$, where T is the oscillation time scale. If acceleration by E_r is dominant in equation (3), $v_y \sim -(eE_r/m)t_a$. Then, using the quarter meandering period $t_{qm} = a^{1/3}$, we obtain $T^{-1} \sim (eb/mc)^{1/2}(eE_r t_a/m)^{1/2} = t_{qm}^{-1}(t_a/t_{qm})^{1/2}$. When the particle arrives at $z = z_a$ for the first time from $z = 0$, the arrival time t_a is close to t_{qm}, resulting in T~t_{qm}. Therefore, the amplitude $z_a T^{-1}$~z_a/t_{qm}, which simply represents the travel speed from $z = 0$ to $z = z_a$ during the meandering motion. As the bounce motion continues, v_y increases; therefore, the amplitude $z_a T^{-1}$~$z_a(eb/mc)^{1/2}(-v_y)^{1/2}$ increases. In addition, the cotangent function appears, because both z and v_z oscillate as time t increases, and we measure v_z at the fixed position $z = z_a$. Since the particle's $v_y \propto t$, the v_z oscillation is expressed as a function of v_y.

Equation (8) describes the position of a particle in the v_y-v_z plane, but we can discuss a VDF by collecting multiple electron positions in the velocity plane. Equation (8) represents multiple curves in a VDF at $z = z_a$, and these are mapped from the line $v_{y0} = const.$ in the VDF at $z = 0$. The velocity v_z becomes 0 at multiple points where the argument of cotangent equals to $(2n - 1)\pi/2$, where n is an integer, while v_z^2 becomes infinity when the argument becomes $(n - 1)\pi$.

The separation of stripes (Δv_y) for a nonrelativistic case (γ~1) is obtained from $v_z = 0$ points in equation (8). Considering (n + 1)th stripe and nth stripe, the separation Δv_y for those two curves on $v_z = 0$ is

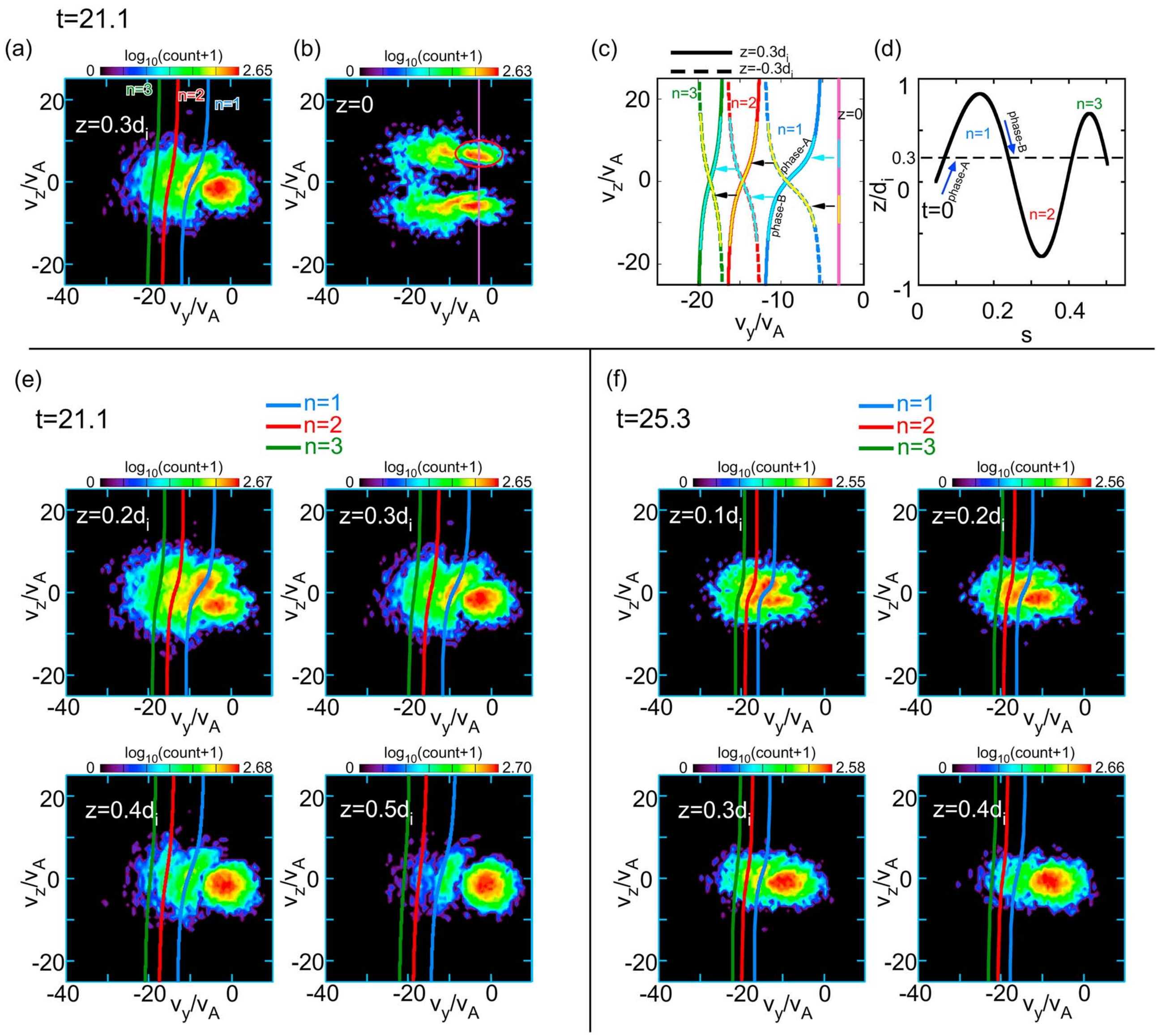

Figure 2. (a) Reduced VDF in v_y-v_z at $z = 0.3d_i$, and theoretical curves (blue: $n = 1$, red: $n = 2$, and green: $n = 3$). (b) Reduced VDF at the X-line ($z = 0$). Oval: zero-bounce population. Purple line: $v_y = v_{y0}$. (c) Mapping from the light-blue segments in the purple line at $z = 0$. Thick curves: mapping at $z = 0.3d_i$. Dashed curves at $z = -0.3d_i$. (d) z oscillation. $n = 1$ and $n = 3$ in $z > 0$, and $n = 2$ in $z < 0$. (e, f) Comparisons of the theory with VDFs at $\Omega_i t = 21.1$ and 25.3. $n = 1$ (blue), $n = 2$ (red), and $n = 3$ (green). VDF = velocity distribution function.

$$\Delta v_y = \left[\left(-v_{y0} - \frac{ck}{b}\right)^{3/2} + \frac{3\pi}{4}(2n+1)\left(\frac{mc}{eb}\right)^{1/2}\frac{eE_r}{m}\right]^{2/3} - \left[\left(-v_{y0} - \frac{ck}{b}\right)^{3/2} + \frac{3\pi}{4}(2n-1)\left(\frac{mc}{eb}\right)^{1/2}\frac{eE_r}{m}\right]^{2/3}. \tag{9}$$

The separation becomes larger as E_y increases. Δv_y should be greater than the thermal spread of the initial stripe at $v_y = v_{y0}$, when a VDF has multiple stripes.

Figure 2a shows the reduced VDF in v_y-v_z at $z = 0.3d_i$ and x of the X-line at $\Omega_i t = 21.1$, and the curves based on equation (8). We used $b = 0.83B_0/d_i$, $k = 1.1(B_0 v_A/c)/d_i$, $E_r = 0.76B_0 v_A/c$, and $v_{y0} = -3v_A$ (b and k are measured from the dashed red and blue lines in Figure 1a). The curves (blue, red, and green, corresponding to $n = 1$, 2, and 3, respectively) well match each crescent stripe, and the cotangent curves well explain the stripe separation as well as higher energy in $v_z < 0$ due to acceleration by E_y.

Let us discuss a mapping from $v_y = v_{y0} = const.$ at $z = 0$ to a curve (equation (8)) at general z. Figure 2b is the X-line VDF (at $z = 0$) at $\Omega_i t = 21.1$. There are two layers ($v_z > 0$ and $v_z < 0$), and we regard the rightmost population (an oval) as electrons just arriving at $z = 0$ from $z < 0$ without meandering. They start meandering toward $z > 0$ with $v_z > 0$. The counterpart ($v_z < 0$) in the lower layer is due to electrons starting meandering toward $z < 0$ with $v_z < 0$. The purple line, $v_{y0} = -3v_A$, passes through the v_y center of the oval, and we use this line to represent this VDF population, in $3.5v_A \le v_z \le 10v_A$ (within the oval). Figure 2c shows the mapping of $v_y = v_{y0} = -3v_A$ at $z = 0$ to each stripe at $z = z_a = 0.3d_i$. The v_z-range ($3.5v_A \le v_z \le 10v_A$, where $v_{z0} = 3.5v_A$ is the least v_{z0} required to reach z=0.3d_i) is drawn as the light-blue segment on the purple line. We consider the mapping of this light-blue segment from $z = 0$ to the curves at $z = z_a = 0.3d_i$. The blue curve ($n = 1$, without dash), obtained using $v_{y0} = -3v_A$ in equation (8), corresponds to the cotangent curve closest to $v_y = -3v_A$, and the light-blue segment in the blue curve is the mapping from the light-blue segment in the purple line. In this curve, v_z becomes 0 when the argument of cotangent becomes $(2n - 1)\pi/2$ with $n = 1$. This integer, $n = 1$, represents the first meandering motion from $z = 0$, as defined in Figure 2d: $n = 1$ motion from the initial $z = 0$ toward $z > 0$ until it returns to $z = 0$. After then, $n = 2$ motion starts toward $z < 0$ until it returns to $z = 0$. In this way, if electrons start with $v_z > 0$ at $t = 0$, an odd (even) n number represents the motion in $z > 0$ ($z < 0$).

During $n = 1$ motion, there are two phases (Figure 2d): In phase-A, the electron approaches $z = z_a = 0.3d_i$ from $z < z_a$. In phase-B, after passing $z = z_a$, it reaches the z-maximum and returns to $z = z_a$. In phase-A, the mapping of the light-blue segment in Figure 2c is in $v_z > 0$ (the light-blue curve in $n = 1$, *phase-A*). After these particles in phase-A pass through $z = z_a = 0.3d_i$, they return to $z = z_a$ in phase-B. They are mapped to the other light-blue segment in the blue curve (in $v_z < 0$, *phase-B*), and the energy in phase-B is greater than that in phase-A, because of acceleration by E_y.

After $n = 1$ motion in $z > 0$, those particles on the blue curve move toward $z < 0$ ($n = 2$ motion). Let us consider $z < 0$, and obtain the VDF mapping curve at $z = -z_a = -0.3d_i$. Since $v_z \propto z$ in equation (8), the cotangent curve at $z = -z_a = -0.3d_i$ for $n = 2$ appears as the dashed red curve (again, the light-blue segment in the dashed red curve represents the mapping range). After $n = 2$ motion, they return to $z > 0$, and the light-blue segment on the green curve ($n = 3$, no dash) shows the mapping for $n = 3$ at $z = z_a = 0.3d_i$.

The above argument can also be applied to the population with $v_z < 0$ at $z = 0$ (the yellow segment on the purple line in Figure 2c). The $n = 1$ and $n = 3$ motions appear as the dashed blue and green curves for $z = -z_a = -0.3d_i$, and $n = 2$ motion appears as the red curve (no dash) for $z = 0.3d_i$. In Figure 2c, the blue, red, and green stripes with no dash are at $z = 0.3d_i$, and $n = 1$ and $n = 3$ stripes are due to particles starting with $v_z > 0$ at $z = 0$ (light-blue segment), and only $n = 2$ stripe is due to particles starting with $v_z < 0$ at $z = 0$ (yellow segment).

Figures 2e and 2f show reduced VDFs at various z (and the same x as the X-line) at $\Omega_i t = 21.1$ and 25.3. The blue, red, and green theoretical curves correspond to $n = 1$, $n = 2$, and $n = 3$ motion. For $\Omega_i t = 25.3$, $b = 0.67B_0/d_i$, $k = 6.1(B_0v_A/c)/d_i$, $E_r = 0.43B_0v_A/c$, and $v_{y0} = -12v_A$. The theory predicts that the closer the measurement point is to $z = 0$, the more significant bent appears. Also, the striation separations become larger as E_y increases (see equation (9)). If we compare (e) ($\Omega_i t = 21.1$) and (f) ($\Omega_i t = 25.3$), the separations at $\Omega_i t = 21.1$ ($E_y = 0.76B_0v_A/c$) are overall larger than those at $\Omega_i t = 25.3$ ($E_y = 0.43B_0v_A/c$). These tendencies are consistent with the VDFs in the simulation. Note that in the theory, we assume that the second last term in equation (4) ($\propto z^3$) is negligible; therefore, the theory and the simulation agree in small z. At the farthest position ($z = 0.5d_i$ at $\Omega_i t = 21.1$, and $z = 0.4d_i$ at $\Omega_i t = 25.3$), the theory shows slightly larger $|v_y|$ values (more negative v_y) than stripes in the VDFs. We also note that at $\Omega_i t = 21.1$, the innermost E_z-inversion layer exists near $z = 0$. We performed a test particle analysis using the 1-D field profiles in Figures 1a and 1b and confirmed that the effect of the E_z-inversion structure on the electron VDFs is negligible for the analyzed locations (test particle results not shown).

4. Comparison Between Theory and MMS Observation

In Earth's magnetotail, MMS recently detected electron VDFs with multiple crescents in an EDR observed on 11 July 2017 (Torbert et al., 2018). In MMS, magnetic fields are from Flux Gate Magnetometer (Russell et al.,

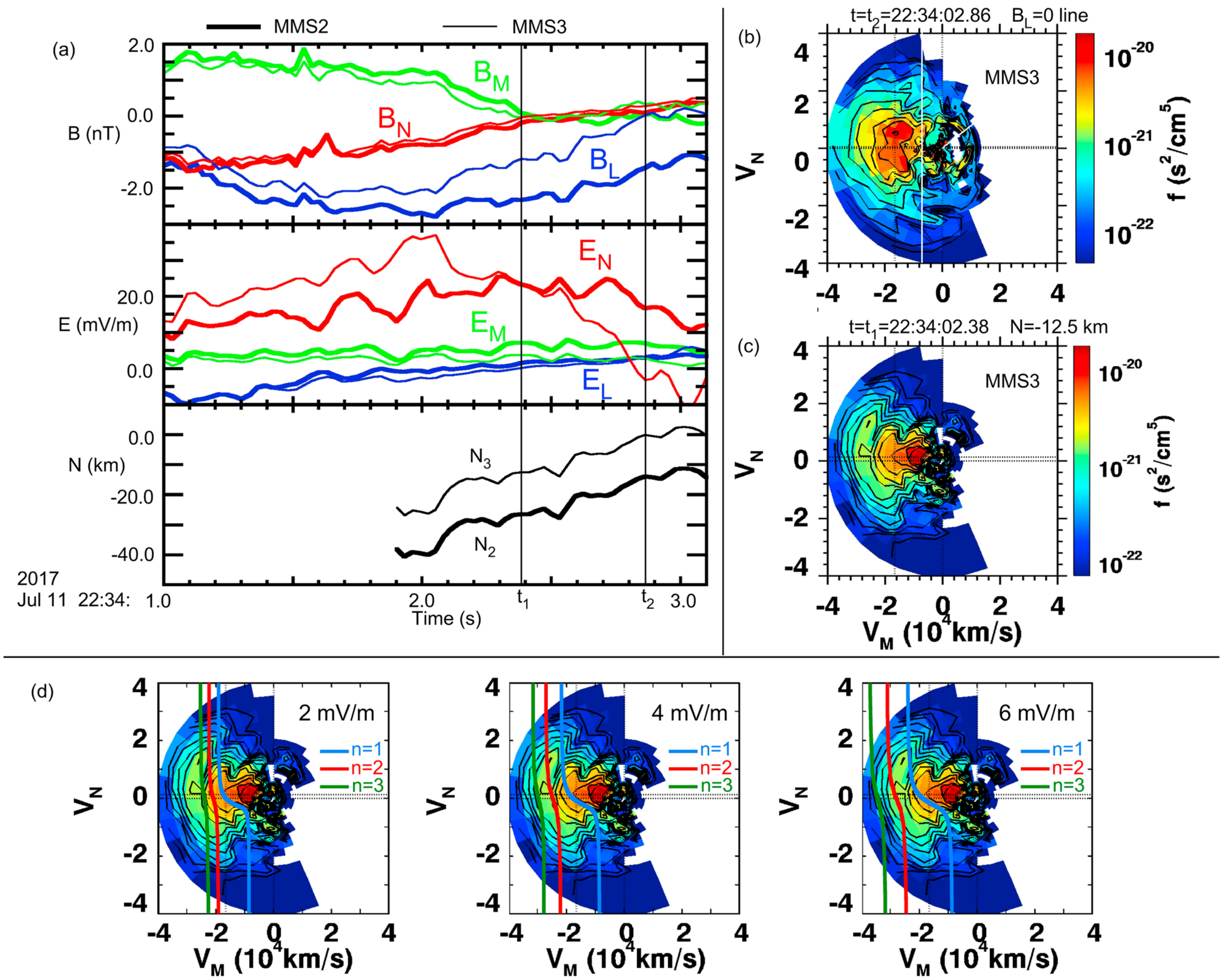

Figure 3. MMS observation of electron diffusion region electron crescents on 11 July 2017. (a) Magnetic and electric fields in *LMN* by MMS2 (thick) and MMS3 (thin), and *N*-distance from $B_L = 0$. MMS3 observed a crescent-VDF at $t = t_1$ and crossed $B_L = 0$ at $t = t_2$. (b, c) Reduced VDFs in v_M-v_N. White line at $t = t_2$ (b): $v_M = v_{M0}$. Panel(c): multiple crescents at $t = t_1$. (d) Comparisons between the theory and MMS3 VDF at $t = t_1$. The curves for $n = 1$ (blue) and $n = 2$ (red) are compared with the observed stripes. $E_M = 4$ mV/m (middle) shows agreement between the theory and the observed stripes. MMS = Magnetospheric Multiscale; VDF = velocity distribution function.

2014), electric fields from double probes in the FIELDS suites (Ergun et al., 2014; Lindqvist et al., 2014; Torbert et al., 2014), and electron VDFs from Fast Plasma Investigation (Pollock et al., 2016). Figure 3a shows an overview of the EDR crossing: time series of magnetic and electric fields measured by MMS2 (thick) and MMS3 (thin), where *LMN* coordinates are *N* (inflow), *L* (outflow), and *M* (out-of-plane), obtained by a hybrid method (Denton et al., 2016) of minimum directional derivative (Shi et al., 2005; for 22:34:01.9–22:34:03.9 UT) and minimum variance analysis (Sonnerup & Scheible, 1998; for 22:34:00–22:34:04), and *N* distances from $B_L = 0$. Magnetic fields (burst mode, 128 samples per second) were smoothed (over 0.03 s, four data points) and interpolated to each electron VDF sampling time with resolution 30 ms. Electric fields (32 samples per second) were also interpolated to the VDF sampling time. *N* distance of MMS3 (N_3) was estimated using a method similar to that employed by Denton et al. (2016), from the integral $\int V_N dt$, where V_N is the MMS barycenter velocity relative to the current sheet, estimated by $V_N = (dB_L/dt)/(dB_L/dN)$ using minimum directional derivative, and *N* distance of MMS2 (N_2) was calculated by $N_2 = N_3 - 13.91$ km, according to the spacecraft positions.

We estimate slopes of B_L and E_N in the *N* direction. Using MMS3 data between 22:34:01.9 and 22:34:03.1 (40 data points), the B_L-slope $b = 9.0 \times 10^{-2}$ nT/km. Also, using MMS2 data between 22:34:02.68 and 22:34:03.1

(14 data points), during which E_N decreases, the E_N-slope $-k = 1.2 \times 10^3$ mV/km^2. During this event, MMS2 shows the best match between $E \times B$ drift and the electron perpendicular speed near the EDR edge (not shown); therefore, the estimate of k is most reliable using MMS2 data.

Figure 3b shows an electron VDF (reduced in v_M-v_N) by MMS3 near $B_L = 0$ ($t = t_2$= 22:34:02.86, the right vertical line in Figure 3a). There are multiple stripes, and we regard the population near the white vertical line as the v_{M0} electrons (zero bounce), $v_{M0} = -0.7 \times 10^4$ km/s. Compared with v_{M0}, the $E_N \times B_L$ drift ($-k/b$) is -1.3×10^4 km/s; therefore, $v_{M0} > -k/b$ (the theory in section 3 is in cgs unit, and taking away c in the formula gives the theory in SI unit). We note that even considering uncertainty in v_{M0} (~30%, not shown), the relation $v_{M0} > -k/b$ holds. Hence, we will use equation (A11) combined with equation (A8).

Figure 3c shows a reduced VDF with multiple crescents by MMS3 at 22:34:02.38 ($t = t_1$, the left vertical line in Figure 3a). At this time, the N distance was $N_3 = -12.5$ km. Three stripes can be seen at v_M~ -0.9×10^4, -1.8×10^4, and -2.8×10^4 km/s. The first stripe (v_M~ -0.9×10^4 km/s) can be interpreted as the inflow population, and the second and third stripes are meandering electrons.

Let us compare the theory (equations (A8) and (A11)) with this multiple-crescent VDF. Electrons are nonrelativistic, and we use $\gamma = 1$ in the theory. The theory needs N, v_{M0}, b, and k, as estimated above. The last parameter is the reconnection electric field E_M, which is hard to determine by direct E field measurements due to fluctuations around $t = t_1$ and because an averaged E_M is small (3 mV/m, comparable to uncertainty 1–2 mV/m for E_M). In Figure 3d, varying E_M from 2 to 6 mV/m, we compare the theory and the VDF to estimate E_M. The blue, red, and green curves represent $n = 1$, $n = 2$, and $n = 3$ curves, respectively. Note that we plotted $n = 3$ curve, but MMS3 did not observe a clear $n = 3$ population; therefore, let us compare $n = 1$ and $n = 2$ curves with the observed second and third stripes in the VDF (v_M~ -1.8×10^4 and -2.8×10^4 km/s, respectively). When $E_M = 2$ mV/m (left), $n = 1$ curve (blue) is at the observed second stripe, but $n = 2$ curve (red) does not match the observed third stripe (the red curve passes through the second stripe instead). When $E_M = 4$ mV/m (middle), both $n = 1$ and $n = 2$ curves match the observed second and third stripes. When $E_M = 6$ mV/m (right), $n = 1$ (blue) curve in $v_N < 0$ matches the observed second stripe, but the blue curve in $v_N > 0$ passes through the third stripe, too. Also, $n = 2$ curve (red) does not match the observed third stripe very well. We also compared with $E_M = 5$ mV/m (not shown), and it is also consistent with the VDF. We conclude that the reconnection electric field is 4–5 mV/m, close to 3 mV/m observed by MMS3 around $t = t_1$, considering uncertainty 1–2 mV/m in the measurement.

5. Conclusion

We have discussed electron motion in the EDR in symmetric reconnection and examined the overall shape of electron distributions, including an equation for stripes (crescents) in a VDF. Electrons meander across the current sheet, and their speed in the current direction $|v_y|$ increases due to the reconnection electric field E_y. When combined with an oscillation in the direction normal to the current layer (z), the resulting motion leads to the formation of a tilted multiple-crescent VDF in the v_y-v_z plane. The shape of crescents is obtained as a function of fields (slopes of B_x and E_z, and the strength of E_y), the distance from $z = 0$, and the initial v_y at $z = 0$. As E_y increases, the separation between stripes becomes larger. We have compared the theory with a crescent VDF observed by MMS in Earth's magnetotail and estimated the reconnection electric field as 4–5 mV/m.

Appendix A: Derivation of v_y-v_z Relation

In equation (5), we use the following approximations: $\mathrm{Ai}(-a^{1/3}s)$~ $\cos[(2/3)a^{1/2}s^{3/2} - \pi/4]/(\pi^{1/2}a^{1/12}s^{1/4})$ and $\mathrm{Bi}(-a^{1/3}s)$~ $-\sin[(2/3)a^{1/2}s^{3/2} - \pi/4]/(\pi^{1/2}a^{1/12}s^{1/4})$. These are valid only for $s > 0$. Note that when $t = 0$, $s = s_0 = -(m/eE_r)(v_{y0} + ck/b)$. Let us assume that $s_0 > 0$, that is, $v_{y0} < -ck/b$.

Using the approximations, z in equation (5) becomes

$$z \sim \frac{\left(c_1^2 + c_2^2\right)^{1/2}}{\pi^{1/2} a^{1/12} s^{1/4}} \sin\left[\frac{2}{3} a^{1/2} s^{3/2} - \frac{\pi}{4} + \tan^{-1}\left(\frac{c_1}{|c_2|}\right)\right], \tag{A1}$$

where we assumed $c_1 \geq 0$ and $c_2 \leq 0$, and $0 \leq \tan^{-1}(c_1/|c_2|) \leq \pi/2$. Taking the time derivative (d/dt = d/ds), we have

$$v_z \sim \frac{\left(c_1^2 + c_2^2\right)^{1/2}}{\pi^{1/2} a^{1/12} s^{1/4}} \cos\left[\frac{2}{3} a^{1/2} s^{3/2} - \frac{\pi}{4} + \tan^{-1}\left(\frac{c_1}{|c_2|}\right)\right] a^{1/2} s^{1/2} - \frac{1}{4}\frac{z}{s}. \tag{A2}$$

Considering $z = 0$ and $v_z = v_{z0}$ at $t = 0$, let us determine c_1 and c_2. In equation (A1), substituting $z = 0$ and $t = 0$ ($s = s_0$), we have

$$\frac{2}{3} a^{1/2} s_0^{3/2} - \frac{\pi}{4} + \tan^{-1}\left(\frac{c_1}{|c_2|}\right) = l\pi, \tag{A3}$$

where l is an integer. Taking $l = 0$ in equation (A3), we obtain

$$c_1 = |c_2| \tan\left(\frac{\pi}{4} - \frac{2}{3} a^{\frac{1}{2}} s_0^{\frac{3}{2}}\right). \tag{A4}$$

Substituting equation (A4) into equations (A1) and (A2), z and v_z are

$$z \sim \frac{|c_2|}{\pi^{1/2} a^{1/12} s^{1/4}} \sec\left[\frac{\pi}{4} - \frac{2}{3} a^{1/2} s_0^{3/2}\right] \sin\left[\frac{2}{3} a^{1/2}\left(s^{3/2} - s_0^{3/2}\right)\right], \tag{A5}$$

$$v_z \sim \frac{|c_2|}{\pi^{1/2} a^{1/12} s^{1/4}} \sec\left[\frac{\pi}{4} - \frac{2}{3} a^{1/2} s_0^{3/2}\right] \cos\left[\frac{2}{3} a^{1/2}\left(s^{3/2} - s_0^{3/2}\right)\right] a^{1/2} s^{1/2} - \frac{1}{4}\frac{z}{s}. \tag{A6}$$

c_2 is determined by $v_z(t = 0) = v_{z0}$, using equation (A6). However, in the following discussion aiming to obtain the relation between v_y and v_z, we do not need to obtain c_2. Instead, from equations (A5) and (A6), we obtain

$$v_z \sim z a^{1/2} s^{1/2} \cot\left[\frac{2}{3} a^{1/2}\left(s^{3/2} - s_0^{3/2}\right)\right], \tag{A7}$$

where we neglected a small term (1/4)z/s in equation (A6). The right-hand side $\propto z$, but this does not mean $v_z = 0$ when $z = 0$ at $t = 0$. Since the argument of sine in z becomes zero when $t = 0$, the cotangent in equation (A7) becomes infinity at $t = 0$. Therefore, v_z remains nonzero at $t = 0$.

The v_y-v_z relation is obtained from equation (A7) by expressing s with v_y. Using equations (7) and (3), we have

$$s = -\frac{m}{eE_r}\left(\gamma v_y + \frac{eb}{2mc} z^2 + \frac{ck}{b}\right), \tag{A8}$$

where $\gamma = 1 + (1/2)(v_y/c)^2$. Substituting equation (A8) into (A7), we obtain the v_y-v_z relation, equation (8) in section 3.

In the above, $s_0 > 0$ (i.e., $v_{y0} < -ck/b$) is assumed; however, in general, $s_0 \leq 0$ ($v_{y0} \geq -ck/b$) can occur, and in that case, we cannot apply the above theory. We can discuss such cases using Airy functions without approximations. Using equation (5), we obtain

$$z = \frac{\pi v_{z0}}{a^{1/3}}\left(\mathrm{Bi}_0\mathrm{Ai} - \mathrm{Ai}_0\mathrm{Bi}\right), \tag{A9}$$

and

$$v_z = -\pi v_{z0}\left(\mathrm{Bi}_0\mathrm{Ai}' - \mathrm{Ai}_0\mathrm{Bi}'\right), \tag{A10}$$

where Ai and Bi are $\mathrm{Ai}(-a^{1/3}s)$ and $\mathrm{Bi}(-a^{1/3}s)$, and Ai' and Bi' are derivatives $d\mathrm{Ai}(x)/dx|_{x=-a^{1/3}s}$ and

$d\text{Bi}(x)/dx|_{x=-a^{1/3}s}$, respectively. The subscript 0 represents the values at $s = s_0$. From equations (A9) and (A10), eliminating v_{z0}, we obtain

$$v_z = za^{1/3}\frac{\text{Bi}_0\text{Ai}' - \text{Ai}_0\text{Bi}'}{\text{Ai}_0\text{Bi} - \text{Bi}_0\text{Ai}}. \quad \text{(A11)}$$

In equation (A11), Airy functions are functions of $-a^{1/3}s$; therefore, we use equation (A8) to convert s to v_y. Combining with equation (A8), equation (A11) gives the v_z-v_y relationship for general s_0. Equation (A11) approaches to equation (8) if $s_0 > 0$.

Acknowledgments

The work was supported by DOE grant DESC0016278, NSF grants AGS-1619584 and AGS-1552142, NASA grant 80NSSC18K1369, and the NASA MMS project. Work at the University of Bergen was supported by the Research Council of Norway/CoE under contract 223252/F50. PIC simulations were performed on Pleiades at the NASA Advanced Supercomputing, and subsets of simulation data are available from The Digital Repository at the University of Maryland (DRUM; http://hdl.handle.net/1903/21408). MMS data are available at the MMS Science Data Center (https://lasp.colorado.edu/mms/sdc/public/).

References

Argall, M. R., Paulson, K., Alm, L., Rager, A., Dorelli, J., Shuster, J., et al. (2018). Electron dynamics within the electron diffusion region of asymmetric reconnection. *Journal of Geophysical Research: Space Physics*, *123*(1), 146–162. https://doi.org/10.1002/2017JA024524

Bessho, N., Chen, L.-J., & Hesse, M. (2016). Electron distribution functions in the diffusion region of asymmetric magnetic reconnection. *Geophysical Research Letters*, *43*, 1828–1836. https://doi.org/10.1002/2016GL067886

Bessho, N., Chen, L.-J., Hesse, M., & Wang, S. (2017). The effect of reconnection electric field on crescent and U-shaped distribution functions in asymmetric reconnection with no guide field. *Physics of Plasmas*, *24*, 072903. https://doi.org/10.1063/1.4989737

Bessho, N., Chen, L.-J., Shuster, J. R., & Wang, S. (2014). Electron distribution functions in the electron diffusion region of magnetic reconnection: Physics behind the fine structures. *Geophysical Research Letters*, *41*, 8688–8695. https://doi.org/10.1002/2014GL062034

Birn, J., Drake, J. F., Shay, M. A., Rogers, B. N., Denton, R. E., Hesse, M., et al. (2001). Geospace Environmental Modeling (GEM) magnetic reconnection challenge. *Journal of Geophysical Research*, *106*, 3715–3719. https://doi.org/10.1029/1999JA900449

Burch, J. L., Moore, T. E., Torbert, R. B., & Giles, B. L. (2015). Magnetospheric Multiscale overview and science objectives. *Space Science Reviews*, *199*, 5.

Burch, J. L., & Phan, T. D. (2016). Magnetic reconnection at the dayside magnetopause: Advances with MMS. *Geophysical Research Letters*, *43*, 8327–8338. https://doi.org/10.1002/2016GL069787

Burch, J. L., Torbert, R. B., Phan, T. D., Chen, L. J., Moore, T. E., Ergun, R. E., et al. (2016). Electron-scale measurements of magnetic reconnection in space. *Science*, *12*, aaf2939.

Cassak, P. A., Genestreti, K. J., Burch, J. L., Phan, T.-D., Shay, M. A., Swisdak, M., et al. (2017). The effect of a guide field on local energy conversion during asymmetric magnetic reconnection: Particle-in-cell simulations. *Journal of Geophysical Research: Space Physics*, *122*, 11,523–11,542. https://doi.org/10.1002/2017JA024555

Chen, L.-J., Daughton, W. S., Lefebvre, B., & Torbert, R. B. (2011). The inversion layer of electric fields and electron phase-space-hole structure during two-dimensional collisionless magnetic reconnection. *Physics of Plasmas*, *18*, 012904. https://doi.org/10.1063/1.3529365

Chen, L.-J., Hesse, M., Wang, S., Bessho, N., & Daughton, W. (2016). Electron energization and structure of the diffusion region during asymmetric reconnection. *Geophysical Research Letters*, *43*, 2405–2412. https://doi.org/10.1002/2016GL068243

Chen, L.-J., Hesse, M., Wang, S., Gershman, D., Ergun, R., Pollock, C., Torbert, R., et al. (2016). Electron energization and mixing observed by MMS in the vicinity of an electron diffusion region during magnetopause reconnection. *Geophysical Research Letters*, *43*, 6036–6043. https://doi.org/10.1002/2016GL069215

Chen, L.-J., Hesse, M., Wang, S., Gershman, D., Ergun, R. E., Burch, J., et al. (2017). Electron diffusion region during magnetopause reconnection with an intermediate guide field: Magnetospheric Multiscale observations. *Journal of Geophysical Research: Space Physics*, *122*, 5235–5246. https://doi.org/10.1002/2017JA024004

Daughton, W., Scudder, J., & Karimabadi, H. (2006). Fully kinetic simulations of undriven magnetic reconnection with open boundary conditions. *Physics of Plasmas*, *13*, 072101. https://doi.org/10.1063/1.2218817

Denton, R. E., Sonnerup, B. U. Ö., Hasegawa, H., Phan, T. D., Russell, C. T., Strangeway, R. J., et al. (2016). Motion of the MMS spacecraft relative to the magnetic reconnection structure observed on 16 October 2015 at 1307 UT. *Geophysical Research Letters*, *43*, 5589–5596. https://doi.org/10.1002/2016GL069214

Divin, A., Markidis, S., Lapenta, G., Semenov, V. S., Erkaev, N. V., & Biernat, H. K. (2010). Model of electron pressure anisotropy in the electron diffusion region of collisionless magnetic reconnection. *Physics of Plasmas*, *17*, 122102. https://doi.org/10.1063/1.3521576

Egedal, J., Le, A., Daughton, W., Wetherton, B., Cassak, P. A., Chen, L.-J., Lavraud, B., et al. (2016). Spacecraft observations and analytic theory of crescent-shaped electron distributions in asymmetric magnetic reconnection. *Physical Review Letters*, *117*, 185101. https://doi.org/10.1103/PhysRevLett.117.185101

Ergun, R. E., Tucker, S., Westfall, J., Goodrich, K. A., Malaspina, D. M., Summers, D., et al. (2014). The axial double probe and fields signal processing for the MMS mission. *Space Science Reviews*, *199*, 167.

Genestreti, K. J., Burch, J. L., Cassak, P. A., Torbert, R. B., Ergun, R. E., Varsani, A., et al. (2017). The effect of a guide field on local energy conversion during asymmetric magnetic reconnection: MMS observations. *Journal of Geophysical Research: Space Physics*, *122*, 11,342–11,353. https://doi.org/10.1002/2017JA024247

Genestreti, K. J., Varsani, A., Burch, J. L., Cassak, P. A., Torbert, R. B., Nakamura, R., et al. (2018). MMS observation of asymmetric reconnection supported by 3-D electron pressure divergence. *Journal of Geophysical Research: Space Physics*, *123*, 1806–1821. https://doi.org/10.1002/2017JA02501

Hesse, M., Aunai, N., Sibeck, D., & Birn, J. (2014). On the electron diffusion region in planar, asymmetric, systems. *Geophysical Research Letters*, *41*, 8673–8680. https://doi.org/10.1002/2014GL061586

Hesse, M., Liu, Y.-H., Chen, L.-J., Bessho, N., Kuznetsova, M., Birn, J., & Burch, J. L. (2016). On the electron diffusion region in asymmetric reconnection with a guide magnetic field. *Geophysical Research Letters*, *43*, 2359–2364. https://doi.org/10.1002/2016GL068373

Hesse, M., Liu, Y.-H., Chen, L.-J., Bessho, N., Wang, S., Burch, J. L., et al. (2018). The physical foundation of the reconnection electric field. *Physics of Plasmas*, *25*, 032901. https://doi.org/10.1063/1.5021461

Lapenta, G., Berchem, J., Zhou, M., Walker, R. J., El-Alaoui, M., Goldstein, M. L., et al. (2017). On the origin of the crescent-shaped distributions observed by MMS at the magnetopause. *Journal of Geophysical Research: Space Physics*, *122*, 2024–2039. https://doi.org/10.1002/2016JA023290

Lindqvist, P.-A., Olsson, G., Torbert, R. B., King, B., Granoff, M., Rau, D., et al. (2014). The spin-plane double probe electric field instrument for MMS. *Space Science Reviews*, *199*, 137.

Ng, J., Egedal, J., Le, A., & Daughton, W. (2012). Phase space structure of the electron diffusion region in reconnection with weak guide fields. *Physics of Plasmas*, *19*, 112108. https://doi.org/10.1063/1.4766895

Ng, J., Egedal, J., Le, A., Daughton, W., & Chen, L.-J. (2011). Kinetic structure of the electron diffusion region in antiparallel magnetic reconnection. *Physical Review Letters*, *106*, 065002. https://doi.org/10.1103/PhysRevLett.106.065002

Norgren, C., Graham, D. B., Khotyaintsev, Y. V., André, M., Vaivads, A., Chen, L.-J., et al. (2016). Finite gyroradius effects in the electron outflow of asymmetric magnetic reconnection. *Geophysical Research Letters*, *43*, 6724–6733. https://doi.org/10.1002/2016GL069205

Phan, T. D., Eastwood, J. P., Cassak, P. A., Øieroset, M., Gosling, J. T., Gershman, D. J., et al. (2016). MMS observations of electron-scale filamentary currents in the reconnection exhaust and near the X line. *Geophysical Research Letters*, *43*, 6060–6069. https://doi.org/10.1002/2016GL069212

Pollock, C., Moore, T., Jacques, A., Burch, J., Gliese, U., Saito, Y., et al. (2016). Fast Plasma Investigation for Magnetospheric Multiscale. *Space Science Reviews*, *199*, 331–406. https://doi.org/10.1007/s11214-016-0245-4

Rager, A. C., Dorelli, J. C., Gershman, D. J., Uritsky, V., Avanov, L. A., Torbert, R. B., et al. (2018). Electron crescent distributions as a manifestation of diamagnetic drift in an electron-scale current sheet: Magnetospheric Multiscale observations using new 7.5 ms Fast Plasma Investigation moments. *Geophysical Research Letters*, *45*, 578–584. https://doi.org/10.1002/2017GL076260

Russell, C. T., Anderson, B. J., Baumjohann, W., Bromund, K. R., Dearborn, D., Fischer, D., et al. (2014). The Magnetospheric Multiscale magnetometers. *Space Science Reviews*, *199*, 189.

Shay, M. A., Phan, T. D., Haggerty, C. C., Fujimoto, M., Drake, J. F., Malakit, K., et al. (2016). Kinetic signatures of the region surrounding the X line in asymmetric (magnetopause) reconnection. *Geophysical Research Letters*, *43*, 4145–4154. https://doi.org/10.1002/2016GL069034

Shi, Q. Q., Shen, C., Pu, Z. Y., Dunlop, M. W., Zong, Q.-G., Zhang, H., et al. (2005). Dimensional analysis of observed structures using multipoint magnetic field measurements: Application to Cluster. *Geophysical Research Letters*, *32*, L12105. https://doi.org/10.1029/2005GL022454

Shuster, J. R., Chen, L.-J., Hesse, M., Argall, M. R., Daughton, W., Torbert, R. B., & Bessho, N. (2015). Spatiotemporal evolution of electron characteristics in the electron diffusion region of magnetic reconnection: Implications for acceleration and heating. *Geophysical Research Letters*, *42*, 2586–2593. https://doi.org/10.1002/2015GL063601

Sonnerup, B. U. Ö., & Scheible, M. (1998). Minimum and maximum variance analysis. In G. Paschmann & P. W. Daly (Eds.), *Analysis methods for multi-spacecraft data*, ISSI. Sci. Rep. SR-001 (pp. 185–220). Noordwijk, Netherlands: ESA Publ.

Speiser, T. W. (1965). Particle trajectories in model current sheets: 1. Analytical solutions. *Journal of Geophysical Research*, *70*(17), 4219–4226. https://doi.org/10.1029/JZ070i017p04219

Torbert, R. B., Burch, J. L., Phan, T. D., Hesse, M., Argall, M. R., Shuster, J., et al. (2018). Electron-scale dynamics of the diffusion region during symmetric magnetic reconnection in space, *Physics* arXiv:1809.06932 [physics.space-ph]

Torbert, R. B., Russell, C. T., Magnes, W., Ergun, R. E., Lindqvist, P.-A., LeContel, O., et al. (2014). The FIELDS instrument suite on MMS: Scientific objectives, measurements, and data products. *Space Science Reviews*, *199*, 105.

Zenitani, S., Hasegawa, H., & Nagai, T. (2017). Electron dynamics surrounding the X line in asymmetric magnetic reconnection. *Journal of Geophysical Research: Space Physics*, *122*, 7396–7413. https://doi.org/10.1002/2017JA023969